Optics & Laser Technology 163 (2023) 109395

Contents lists available at ScienceDirect

Optics and Laser Technology

journal homepage: www.elsevier.com/locate/optlastec

Full length article

Coaxial and synchronous monitoring of molten pool height, area, and temperature in laser metal deposition

Simone Maffia *, Valentina Furlan, Barbara Previtali

Department of Mechanical Engineering, Politecnico di Milano, Via La Masa 1, 20156 Milan, Italy

ARTICLE INFO

Keywords:
Laser metal deposition
Directed energy deposition
Coaxial process monitoring
Molten pool height
Molten pool area
Molten pool temperature

ABSTRACT

Laser Metal Deposition is an additive manufacturing technology that enables to realize of one-of-a-kind large components with a free-form geometry. However, the advantages of laser metal deposition from the economic and sustainability points of view can be attenuated by the presence of defects in the realized components. The process should be real-time monitored to immediately identify the onset of defects or process drifts that may undermine the outcome of the build, also enabling the possibility to immediately act against them with feedback control. Many of the proposed solutions in monitoring the Laser Metal Deposition process exploit the use of only one sensor or more but decoupled ones, which does not provide a comprehensive overview of the process. In this work, a coaxial multi-sensor monitoring system is proposed and exploited to capture the variation of three different process signatures. A custom laser triangulator, a near-infrared camera and a ratio pyrometer for simultaneous monitoring of the molten pool height, molten pool area, and molten pool temperature, respectively, are coaxially integrated. Thanks to the possibility to extract concurrent (in spatial and time domains) signals directly from the workpiece area and in real-time, a comprehensive status of the deposition can be deduced. The influence of the process parameters on the sensed outputs is investigated, and the relationships between the process signatures can be researched. While the molten pool area and its temperature are mostly affected by the laser power, the scan speed is more impactful on the molten pool height. A good linear correlation between the molten pool temperature and the area is assessed, while no correlation with the molten pool height is found, making it almost independently manipulatable.

1. Introduction

Additive Manufacturing (AM) is suitable for realizing, repairing, and remanufacturing components made of critical materials, such as titanium alloys, cobalt-based and nickel-based superalloys, and high strength steels [1] in high-end sectors, such as biomedical, aerospace, oil and gas as well as tools and machinery. Among AM technologies, the Laser Metal Deposition (LMD) process is a good candidate to be adopted in the supply chain of the abovementioned components, thanks to the good compromise between high deposition rate, high density, and geometrical accuracy it can reach. Indeed, the high deposition rate allows to reduce the lead time, which is a fundamental requirement from the economic and sustainability standpoints, given the high cost of the abovementioned materials and of the realized objects [2,3].

Nevertheless, LMD is very complex due to the huge amount of controllable and uncontrollable factors governing the process, starting from the process parameters up to the final component geometry and dimension [4]. One of the main concerns of the introduction of LMD into the supply chain of functional parts for demanding sectors, such as the aerospace and the oil and gas industries, is the reliability and reproducibility of the process to meet the high standards of these two fields [5]. Indeed, some instabilities or drifts from the optimal build conditions may occur during the LMD process. Usually, these can be related to the geometrical characteristics of the component that might not facilitate the dissipation of the heat released by the molten pool. This kind of process drifts can ultimately be detrimental to the geometrical accuracy of the realized unit [6], or they can determine the formation of internal metallurgical defects [7]. These phenomena are often unpredictable, or the required simulation effort may be excessive, like in the case of small batches or one-of-a-kind components. For guaranteeing the stability of the process and the optimal deposition conditions against possible unpredicted drifts, the implementation of monitoring or control systems is necessary [8], in particular when large components have to be manufactured. In this case, indeed, the LMD process is usually tuned and

* Corresponding author.
E-mail address: simone.maffia@polimi.it (S. Maffia).

https://doi.org/10.1016/j.optlastec.2023.109395
Received 30 December 2022; Received in revised form 20 February 2023; Accepted 16 March 2023
Available online 6 April 2023
0030-3992/© 2023 The Authors. Published by Elsevier Ltd. This is an open access article under the CC BY license (http://creativecommons.org/licenses/by/4.0/).

validated on sample geometries that are necessarily limited in size and very different from the real components that LMD is meant to realize or repair, which would probably be larger and have more complex features, and thus a different and not homogeneous thermal cycle [9–11]. Through the usage of monitoring systems, process drifts from the designed optimal conditions can be detected, allowing for their identification and correction before the conclusion of the build job (namely, open-loop control strategy). On the other hand, feedback control systems continuously act on the process parameters during the deposition trying to maintain the deposition condition inside the designed stability range (namely, closed-loop control strategy) [12].

Among LMD-related research topics, monitoring and controlling the process conditions is arguably one of the most investigated ones, with various proposed solutions [13]. In this field, the most exploited types of sensors are the camera-based ones, working in both the visible and infrared range of the electromagnetic spectrum. The former is mostly used to analyze the geometrical characteristics of the molten pool [14–23] or of the deposited layers [24–26], whereas the latter is used in thermal analysis of the molten pool [27–35]. The analysis of the data coming from camera-based systems needs further elaboration to extract the desired features, like the molten pool width or the thermal profile, by exploiting imaging analysis techniques [23].

Other industrially-graded sensors that are commonly employed for LMD monitoring and control are pyrometers, in single-wavelength or dual-wavelength (ratio) configurations. Pyrometers make it possible to measure the temperature of a target, that in the case of the LMD process is the molten pool, by acquiring its electromagnetic spectral emission [36–43]. Their working principle is based on the black-body radiation laws. In single-wavelength mode, only one range of wavelength is analyzed of the whole spectrum and the temperature of the molten pool is calculated through the material emissivity. When using ratio pyrometers, a wider portion of the emitted radiation is captured and divided into two separate channels and the temperature is computed with no need for knowing the material emissivity in its state [44].

The goal of process monitoring is to link on-line measurable quantities (i.e., the process signatures) to quality outputs and characteristics (i.e., the product quality). The main product qualities addressed by the monitoring and control matters are geometrical accuracy (forming appearance and dimensional accuracy), microstructural properties, and the presence of metallurgical defects [13]. A dimensionally stable molten pool is required to obtain uniform deposited wall sizes since the width and height of the molten pool are directly relatable to the width and height of the deposited layers [17,19,45–48]. It was demonstrated that also the molten pool temperature can be used to spot and correct defects in the dimensional accuracy of thin-walled components due to heat and, consequently, material accumulation in thin walls and cylindrical clad [6,49,50]. The molten pool temperature, and as a consequence the cooling rate of solidified metal, is also greatly affecting the microstructure and the metallurgy of the components [7,14,39]. When the connections between the process signatures and the product quality are assessed with sensing and monitoring, these are consequently implemented in feedback control strategies during the deposition process to obtain stable and designed characteristics [12]. Various solutions were proposed to apply active feedback control during the deposition process. In these instances, a controller should continuously adjust one or more process parameters to keep one or more of the monitored process signatures at the desired level [37,40,41,46,47,51–54]. Monitoring and controlling in LMD are essential for ensuring a stable and defect-free growth of the components. Given the complexity of the process, studying and implementing these solutions is crucial for the widespread industrialization of LMD. Despite the fact that this is a popular topic among researchers, most of the time single sensor setups are proposed, which are unable to provide a comprehensive overview of the process status. Only a few multi-sensor setups are shown, however in these cases, the monitoring equipment is implemented in an off-axis configuration, making the measurements direction dependent and limiting their applicability to simple geometries.

In this work, a monitoring system of three simultaneously working coaxial sensors, applied to the powder-based LMD process, is presented. The three sensors are a custom laser triangulator to measure the standoff distance (SOD) and the molten pool height (derived by the SOD measurement), a near-infrared (NIR) camera to measure the molten pool area, and a ratio pyrometer to measure the molten pool temperature. Since the three can readily recognize overgrowth and undergrowth problems, excessive shrinking or enlargement concerns, and overheating and underheating of the molten pool, this setup can provide extensive insight into the current status of the process. The coaxial implementation of the sensors is more challenging than the off-axis one, but it guarantees that all the captured data are referred to the same point, on the top of the molten pool, for all three devices. Moreover, the coaxial implementation makes the measurements independent from the deposition direction, and the monitoring equipment is also more compact than off-axis systems, not limiting the motion of the machine in realizing complex components. Furthermore, the real-time and simultaneous acquisition of the three sensed variables is also guaranteed, allowing for future implementation of a feedback control strategy.

The developed monitoring system provides a complete in-line overview of the process status in real time, thanks to the three sensors working together on the molten pool. Indeed, through this system, it is possible to rapidly detect and eventually fix characteristics such as overgrowth and undergrowth of the layers, and molten pool size drifts that affect the final deposited track width, but also the molten pool overheat or underheat. Furthermore, thanks to the space and time alignment of the three sensors, the monitoring system allows to directly compare the three sensed process signatures to find their relationships and possible correlations. In particular, the purpose of this research is to investigate an association between the temperature of the molten pool and its height and area. The latter variables are directly influencing the geometrical quality of the deposition, but they are more difficult to measure due to the camera-based sensors required. If a strong relationship between the molten pool temperature and the two sensed quantities is assessed, the temperature may be considered as an indirect estimator of the geometrical accuracy of the build. The advantages that such a relationship would bring are the simplicity and reliability of the usage of a ratio pyrometer in a coaxial configuration than the other two camera-based sensors.

An experimental campaign on thin walls is conducted to investigate the influence of the main process parameters on the three monitored process signatures: the molten pool height, the molten pool area, and the molten pool temperature. By comprehensively analyzing the obtained results, a discussion about the possible implementation of feedback controls in LMD is established, with a comparison of the performances of the three sensors and the possibility of manipulating the process signatures with the variation of laser power and the scan speed. A strong linear relationship is found between the molten pool temperature and its area, and the high influence of the laser power on them is assessed. On the contrary, the molten pool height is found to be more affected by the scan speed than by the laser power, making it almost independently manageable with respect to the other two process signatures.

2. Materials and methods

2.1. Powder and substrates

Inconel 718 (IN718) was selected as the studied material for this work. IN718 is a widely adopted nickel-based superalloy in both the aerospace and the oil and gas fields for the realization of jet engines and gas turbines components that are in direct contact with high-temperature fluids, since it possesses superior mechanical behavior under dynamic solicitations in hostile environments (excellent creep resistance at high temperatures, high toughness and high ductility) [55,56]. The used IN718 powder was produced with a plasma

atomization process by AP&C -GE Additive (Saint-Eustache, CA). The chemical composition of the powder is following the ASTM B637 (grade UNS N07718) standard [57]. The plasma atomization process generates spherical metallic particles, as shown in Fig. 1. The nominal granulometry of the powder is between 25 μm and 45 μm. Fig. 2 shows the particle size distribution of the powder, as measured by a Morphologi 4 optical particle size analyzer form Malvern Panalytical Ltd (Malvern, UK).

The samples were realized on 10 mm thick AISI 304 substrates.

2.2. LMD system

A robotized integrated LMD system by BLM GROUP (Cantù, IT) was used for the experimentation. The setup of the LMD system is composed of a YLS-3000 active fiber laser source from IPG Photonics (Oxford, US) operating at 1070 nm of wavelength and with 3000 W of maximum output power. The core diameters of the feeding and process fibers, which are coupled by a fiber-to-fiber coupler, are 100 μm and 400 μm, respectively. The deposition head is an MWO-I-Powder from KUKA AG (Augsburg, DE). The deposition head is equipped with a collimation lens and a focusing lens characterized by a focal length of 129 mm and 200 mm, respectively. This optical setup allows to have a laser spot with a diameter between 0.7 mm and 3.5 mm on the working plane. A COAX-40-F coaxial nozzle from Fraunhofer ILT (Aachen, DE) is used for conveying the powder to the working plane. A TWIN PF 2/2-MF from GTV Verschleißschutz GmbH (Luckenbach, DE) is employed for powder feeding and processing gasses management. Argon is used for both carrier and shielding gasses. An IRB 4600-45 anthropomorphic 6-axis robot coupled with an IRBP A-250 2-axis positioner by ABB Ltd (Västerås, SE) oversee the deposition head movement and the substrate handling, respectively. Fig. 3 shows the described LMD system.

2.3. Process monitoring setup

Inside the deposition head, between the collimation and the focus lenses, a dichroic mirror that is transparent to the wavelength of the process laser and reflective elsewhere, is placed. It makes a 45° angle with the process laser, reflecting the electromagnetic radiation that is emitted by the molten pool and sending it through a lateral optical door of the deposition head, allowing the monitoring of the process in a coaxial configuration (i.e., coaxially with respect to the process laser). The extracted radiation is sensed by three sensors. A custom-made laser triangulator, a NIR camera and a pyrometer are used to measure the stand-off distance (SOD) and the molten pool height, the molten pool area, and the molten pool temperature, respectively. The molten pool height and its area can be directly correlated to the deposited layer thickness (the dimensions along the build direction) and width (in the horizontal direction perpendicular to the travel direction), respectively.

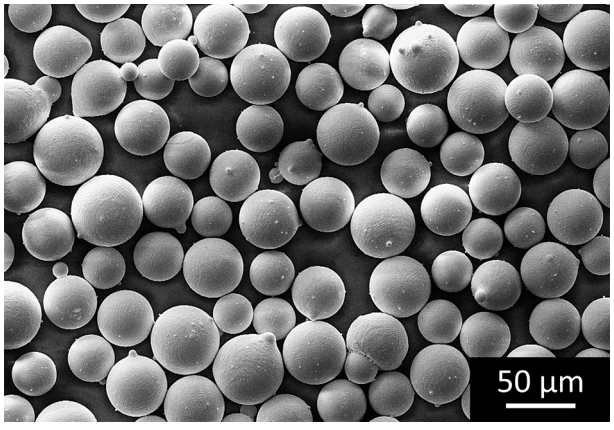

Fig. 1. SEM image of the used IN718 powder.

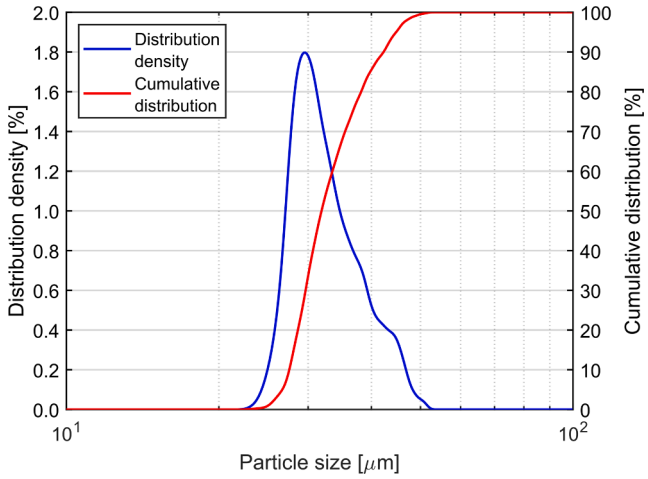

Fig. 2. Particle size distribution of the used IN718 powder.

The laser triangulation system is composed by a green laser probe (CPS532, Thorlabs Inc., Newton, US) and a CMOS camera (XiQ MQ013MG-ON, XIMEA GmbH, Münster, DE). The green laser probe projects a laser beam at 532 nm of wavelength and with 4.5 mW of power through the monitoring optical chain on top of the working plane inside the molten pool. The CMOS camera records the position and displacement of the casted dot on the working plane with respect to the center of the laser spot. After a calibration procedure, the horizontal displacement of the green laser dot can be used to measure the distance between the nozzle tip and the working plane (i.e., the initial SOD). During the deposition process, the green laser is pointed on top of the molten pool. Hence, the measured distance is the one between the nozzle tip and the top of the molten pool (i.e., the actual SOD). A detailed description of the device working principle, calibration, and implementation is found elsewhere [25] and is not reported for the sake of briefness.

The NIR camera system is composed by a CMOS camera (XiQ MQ013MG-ON, XIMEA GmbH, Münster, DE) with a monochromatic sensor. A pair of spectral filters was mounted to select the NIR portion of the electromagnetic spectrum for the molten pool imaging acquisition: a longpass filter with a cut-on wavelength of 850 nm and a shortpass filter with a cut-off wavelength of 1000 nm. The combination of the two filters transmits only the electromagnetic waves that are emitted by the molten pool and have a wavelength included in the selected band (850 nm-1000 nm). An achromatic doublet lens with focal length of 50 mm and an iris diaphragm complete the system.

The pyrometer is a Lascon LPC04, that is a high-speed fiber coupled infrared ratio pyrometer from Dr. Mergenthaler GmbH & Co. KG (Neu-Ulm, DE) operating between 1.60 μm and 2.00 μm split in two channels (1.60 - 1.75 μm and 1.70 - 2.00 μm). Exploiting the two channels, and provided that the grey body assumption holds on the sensed material, ratio pyrometers (calibrated on a black body source) can measure the temperature of the target regardless of its emissivity [44]. This two lambda pyrometer is particularly suitable to be implemented in LMD for monitoring the molten pool temperature since the emissivity of the molten metal is typically not known, but the grey body assumption in the infrared portion of their electromagnetic spectrum can be assumed as valid [44]. With the implemented optical chain, the minimum diameter of the pyrometer field of view is 1.8 mm. However, to match to the laser spot size, the diameter of field of view of the pyrometer, on the working plane, is set to 2.5 mm by adjusting the pyrometer collimation distance.

The coaxial implementation of these three sensors is made possible by using two dichroic mirrors (numbered 6 and 10 in Fig. 4 respectively). The first one, the number 6, is a shortpass dichroic with cut-off wavelength of 650 nm that transmits visible light from and to the

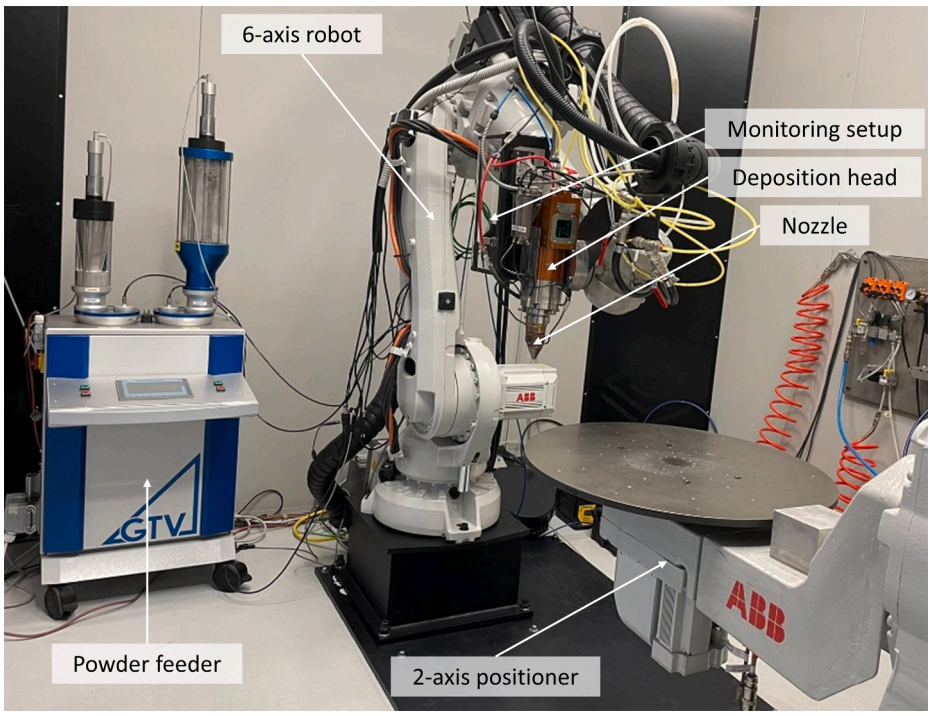

Fig. 3. The LMD system exploited in the experimentation.

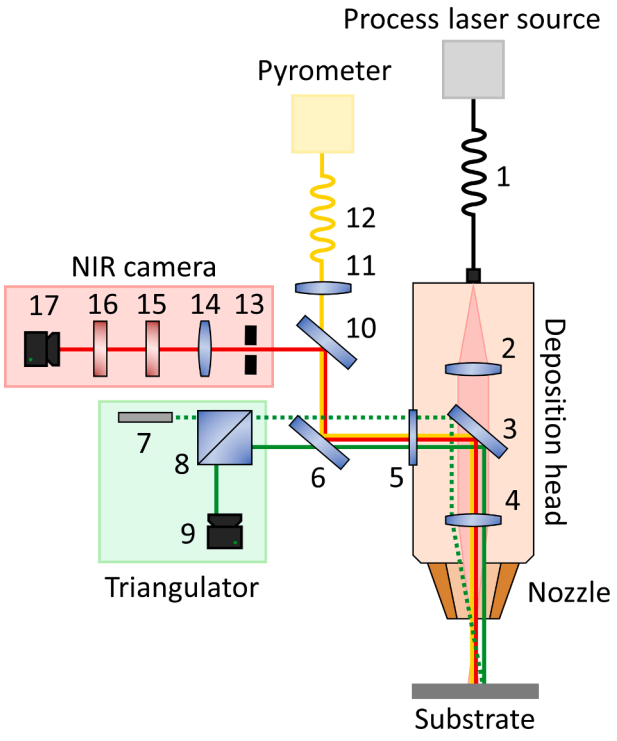

Fig. 4. Optical scheme of the monitoring setup integrated on the deposition head. The triangulator optical scheme is simplified (refer to [25] for the complete version). The numbered elements are: (1) feeding and process fiber (fiber-to-fiber coupler omitted); (2) laser collimation lens; (3) dichroic mirror; (4) laser focusing lens; (5) monitoring optical door; (6) dichroic mirror; (7) green diode laser; (8) beam splitter; (9) CMOS camera; (10) dichroic mirror; (11) pyrometer lens; (12) pyrometer optical fiber; (13) NIR camera iris diaphragm; (14) NIR camera achromatic doublet lens; (15) longpass spectral filter; (16) shortpass spectral filter; (17) CMOS camera. (For interpretation of the references to colour in this figure legend, the reader is referred to the web version of this article.)

triangulator, and it reflects NIR and IR radiations to the pyrometer and the NIR camera. The second one, the number 10, is a longpass dichroic mirror with cut-on wavelength of 1180 nm that transmits IR radiation to the pyrometer, and it reflects NIR radiation to the NIR camera. Fig. 4 shows the optical scheme of the coaxial monitoring setup, and Fig. 5 shows its hardware implementation on the deposition head.

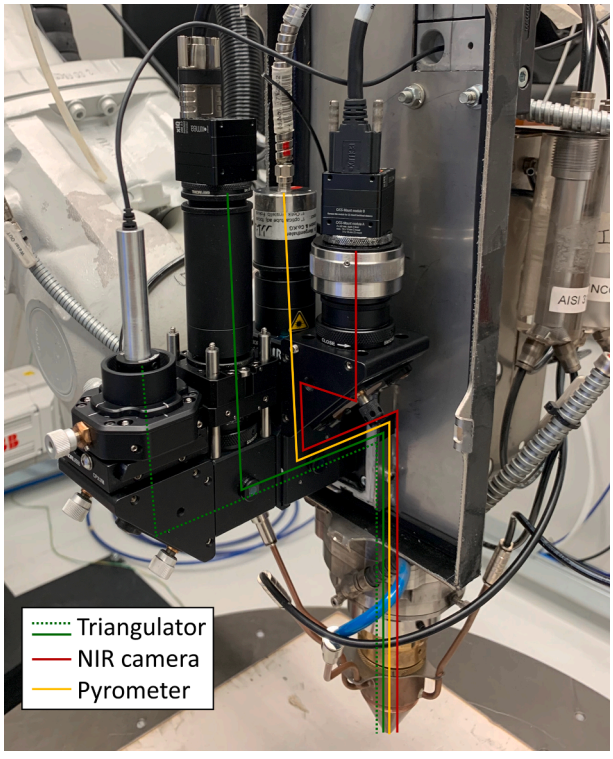

Fig. 5. Hardware implementation of the monitoring system on the deposition head. The optical path of the three sensors is also traced.

2.4. Experimental campaign

A two-factors two-levels experimental campaign with central point was carried out realizing 15 layers high stepped thin-walled samples. The stepped design of the samples was chosen to distinguish the deposited layers for further analysis. Fig. 6 shows a schematic representation of the realized samples. Laser power P and scan speed v were the two investigated factors, while the other process parameters were fixed. A preliminary experimental campaign on single tracks was conducted to tune the best process parameters to allow the realization of the required thin wall samples. The Z-step was selected to guarantee a stable growth in the central point condition of the experimental design. Generally, a stable growth in thin-walled structures (but also in thick-walled ones) is reached when the average layer thickness (not considering the first layer that always grows more than the subsequent ones) matches the imposed Z-step. In the case that the average layer thickness is lower than the set Z-step, underbuilt issues occur, and after few layers the build is lost. In the opposite scenario, the component overgrows, until a new stability point is reached, but the process efficiency is compromised and the energy provided by the laser is lost in overheating the already deposited layers [58]. Table 1 summarizes the experimental design. The process parameters were chosen to obtain three levels of linear energy density E_d: high, medium, and low E_d. The linear energy density is calculated as in Eq. (1), and the scheme of Fig. 7 shows its value for the five combinations of the process parameters.

$$E_d = \frac{P}{v}, \quad \left[\frac{J}{mm}\right] \tag{1}$$

It is worth mentioning that the central point (yellow), the condition with both high P and v (dark orange), and the condition with both low P and v (purple) are characterized by the same E_d, about 70-72 J/mm. A combination of high P and low v (blue) produces the higher E_d, i.e., 100 J/mm. On the contrary, combining low P and high v produces the lower E_d, i.e., 50 J/mm. In this way, it is possible to investigate the effect both of the parameters themselves and of their interaction. Three replicates per condition were realized, obtaining 15 samples. The runs were randomized.

2.5. Process monitoring data acquisition and analysis

The actual SOD, the molten pool area, and its temperature were monitored with the coaxial monitoring setup described in paragraph 2.3. To further improve the triangulator measurement accuracy, on top of the standard static calibration procedure of the device, as reported in [25,26], a dynamic calibration was carried out realizing single tracks with the five process conditions and measuring their height, offsetting the triangulator measurements to match the correct actual SOD. This procedure was necessary since the size of the molten pools that are obtained in this work are larger compared to the previously published experiments [25,26,58], due to the use of more productive but less fine process conditions. Hence, measurement mismatches were recorded between the triangulator and the actual deposited track, and the dynamic calibration was necessary to correct the static calibration. The framerate of the triangulator camera was set to 10 Hz, with an exposure time of 100 ms. The output signal of the triangulator was filtered with a low-pass filter with a 5 layers cut-off to reduce layer-to-layer fast variations, and the SOD was mediated for every layer between the three replicates. The molten pool height of every layer was computed starting from the SOD with Eq. (2):

$$\begin{cases} h(n) = SOD_0 - SOD(n) + Z\text{-}step * (n-1) - \sum_{j=1}^{n-1} h(j), \ [mm] & for\ n \geq 2 \\ h(n) = SOD_0 - SOD(n), \ [mm] & for\ n = 1 \end{cases} \tag{2}$$

where n is the layer number, h is the molten pool height, and SOD_0 is the initial SOD. The molten pool height is considered to be equal to the deposited layer thickness it generates, in accordance to what is common practice in literature [13]. It should be noted that, when the set Z-step between the layers is constant, a layer thickness greater than the Z-step reduces the actual SOD (known as overgrowth condition). On the

Table 1
Process parameters of the experimental campaign.

Fixed parameters	Value	
Z-step, [mm]	0.5	
Initial SOD, [mm]	7	
Laser spot diameter, [mm]	2.5	
Shielding gas flow rate, [L/min]	10	
Carrier gas flow rate, [L/min]	5	
Varied parameters	Levels	Center
Laser power, P [W]	700; 1000	850
Scan speed, v [mm/s]	10; 14	12

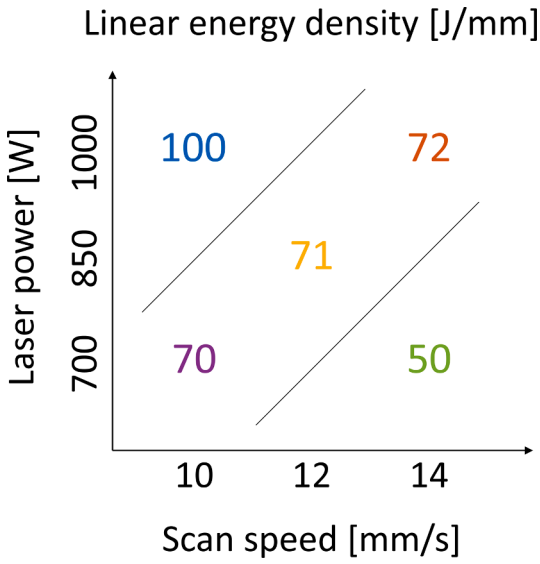

Fig. 7. Scheme of the linear energy density E_d for the five tested process conditions.

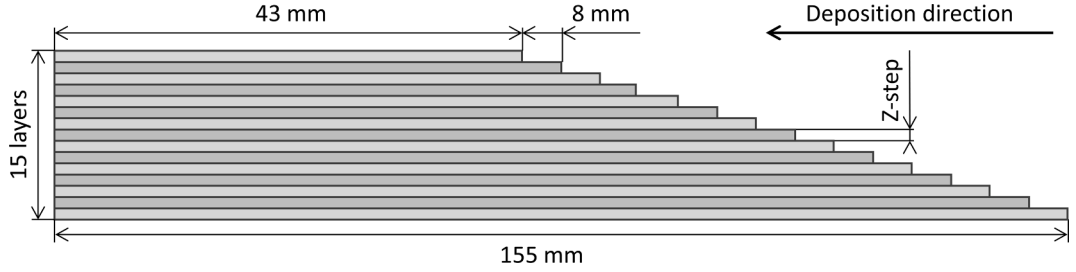

Fig. 6. Schematic representation of the stepped thin-walled samples.

contrary, a layer thickness lower that the Z-step increases the SOD distance (known as undergrowth condition). In the case in which the Z-step perfectly matches the layer thickness, the SOD will remain constant (known as stable condition). During a multi-layer deposition process, the deposition status (overgrowth, undergrowth, and stable growth) is not usually constant and can change between the three described scenarios due to varying thermal conditions and powder catchment efficiency [58].

The NIR camera was also set to an acquisition framerate of 10 Hz and synchronized with the triangulator camera, while the exposure time was set to 0.2 ms. Based on early studies, the camera settings were determined with the goal of identifying acquisition parameters that give satisfactory image quality for all the analyzed process conditions. This strategy was utilized to avoid the acquisition impacting the analysis outcomes. Fig. 8 shows the image processing steps implemented to extract the molten pool area starting from a raw image. The camera acquires 8-bit grayscale pictures in a set rectangular range of interest of 224x224 pixels (Fig. 8a). To improve the molten pool detection quality, the pictures that the NIR camera acquires are treated by applying frame averaging of 5 subsequent frames (Fig. 8b) and denoised using the Wiener filter with a 5x5 pixels neighborhood (Fig. 8c). NIR images of IN718 molten pools are characterized by extremely bright and dark areas. These may impair the molten pool detection capabilities of the algorithm. For this reason, an upper intensity limit is set to the averaged and filtered picture, so that pixels brighter than the imposed limit assume the intensity limit value. Within this work, the intensity limit is set to 51 (Fig. 8d). Due to the coaxial configuration of the monitoring setup, a portion of the internal wall of the nozzle is captured by the NIR camera since it reflects the NIR emission of the molten pool. This may determine an incorrect detection of the molten pool and, therefore, an incorrect measurement of the molten pool area. For this reason, the Circle Hough Transform is implemented to detect the nozzle hole. A circular mask is then applied on the pictures to eliminate the reflection on the nozzle inner wall (Fig. 8e). Finally, the multi-Otsu segmentation method is applied to the masked pictures to identify three segments, the brightest one of which is considered as the molten pool (Fig. 8f). To further clean the obtained binarized image, only the largest white blob is considered and any dark part inside it is filled (Fig. 8g). The area of the molten pool, in pixels, is computed as the total number of white pixels composing the detected molten pool. To obtain the measurement of the area in mm^2, the number of pixels is multiplied by the square of the calibration factor of the camera, which was previously measured by a simple calibration procedure. The calibration factor is 0.02 mm/pixel. The molten pool area signal was filtered using a low–pass filter with a 5 layers cut-off to reduce layer–to–layer fast variations, and it was mediated for every layer between the three replicates. Although the molten pool area detection technique includes numerous steps, it should be noted that all of the applied filters and procedures are mathematically basic and can be processed fast by the dedicated computer. Furthermore, frame averaging is applied to the images continuously, without diminishing the number of elaborated frames in comparison to the acquired ones. The algorithm did provide results faster than the acquisition procedure. Finally, other optimizations such as increasing the framerate or adding adaptive acquisition parameters based on the current process parameters (e.g., adjusting the camera exposure time as a function of the current laser power) might be implemented. [23]).

The pyrometer framerate was set to 50 Hz. The output temperature signal computed by the pyrometer was filtered with a low-pass filter using a 5 layers cut–off to reduce layer-to-layer fast variations, and it was mediated for every layer between the three replicates.

2.6. Statistical analysis

Analysis of variance (ANOVA) and linear correlation analysis techniques are performed on the acquired data using Minitab software from Minitab, LLC (State College, US). The objective of the ANOVA is to inspect the statistical significance of the tested process parameters (the laser power and the scan speed) on the measured process signatures (molten pool height, area and temperature). The current layer is considered as a block factor of the ANOVA to compensate for the variability of the measurements along different layers. On the other hand, the purpose of the correlation analysis is to explore the effect of the molten pool temperature on its height and area. The aim is to investigate the possibility to use the molten pool temperature as an indirect predictor of the deposition height or width. The evidence for these hypotheses would allow using the pyrometer to quantify the deposition height or width through the measurement of the molten pool temperature, without requiring to measure of the molten pool height or area.

3. Results

A picture of the realized specimens is reported in Fig. 9. Fig. 10 and Fig. 11 show the SOD and the molten pool height of the five tested conditions for every layer, respectively.

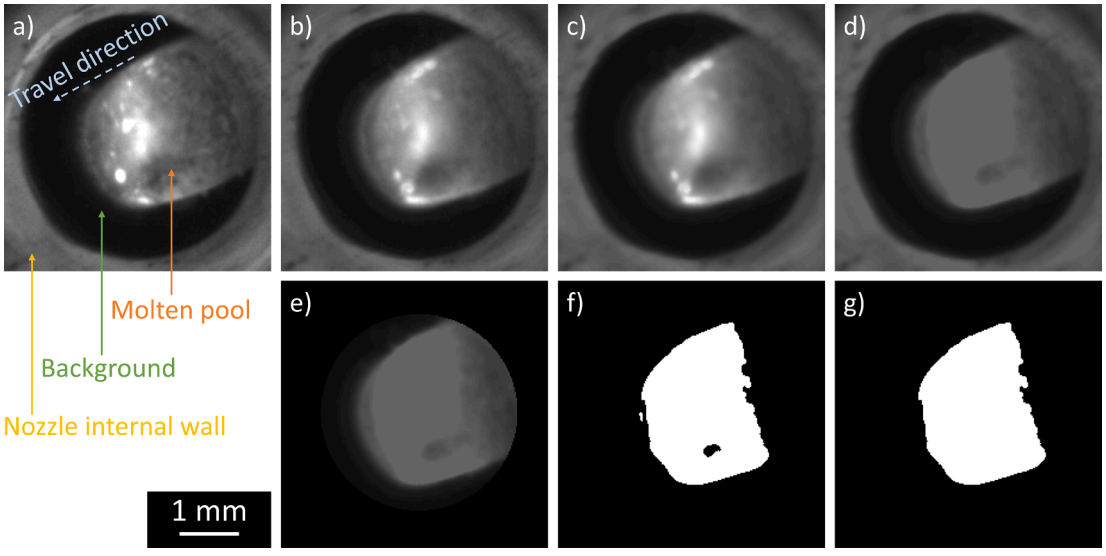

Fig. 8. NIR image treating process: (a) raw image; (b) averaged image; (c) filtered image; (d) intensity-limited image; (e) masked image; (f) binarized image; (g) identified molten pool. To make the representation clearer for the reader, the brightness of the images is increased.

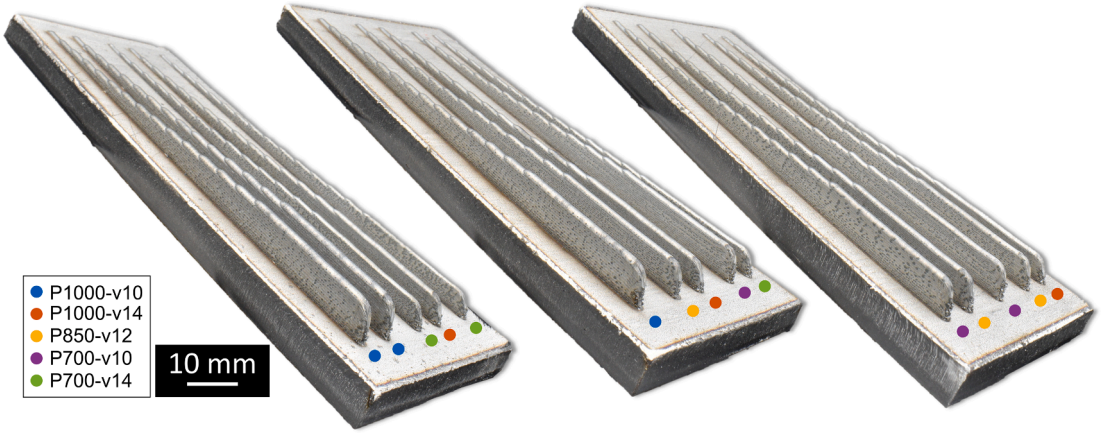

Fig. 9. The fifteen printed thin-walled specimens.

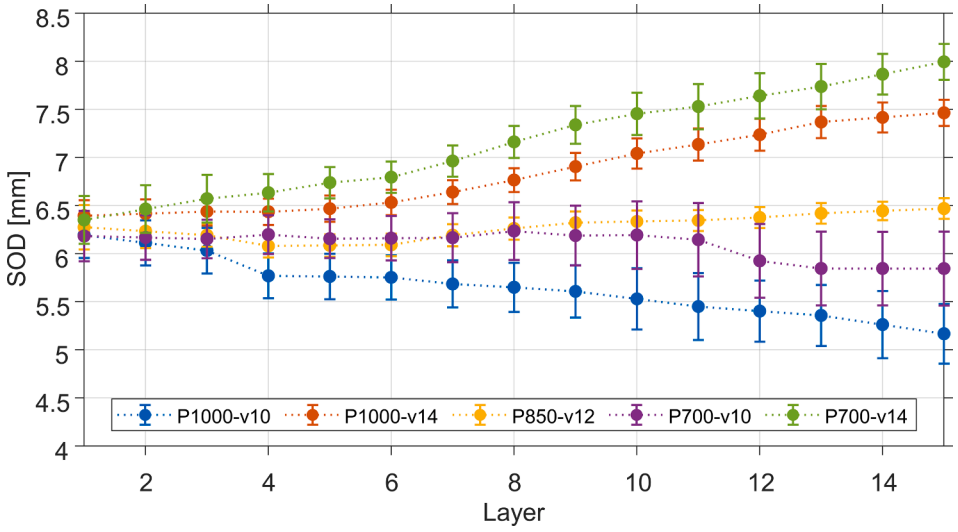

Fig. 10. Median SOD for every layer (error bars represent the mean SOD standard deviation within the layer).

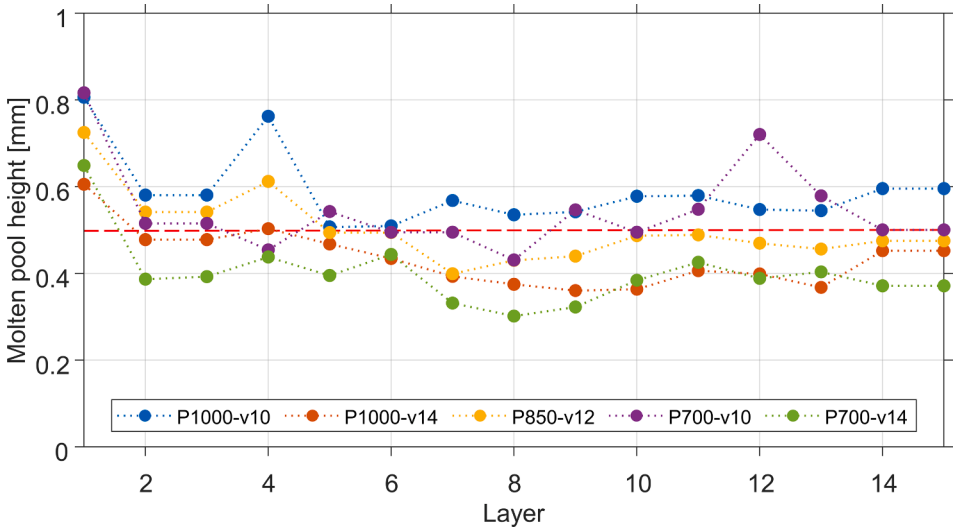

Fig. 11. Median molten pool height for every layer (red dashed line corresponds to the set Z-step between layers). (For interpretation of the references to colour in this figure legend, the reader is referred to the web version of this article.)

Table 2
Average molten pool height of the tested conditions.

Condition	P1000-v10	P1000-v14	P850-v12	P700-v10	P700-v14
Average molten pool height [mm]	0.57 ± 0.06	0.42 ± 0.05	0.49 ± 0.05	0.52 ± 0.07	0.38 ± 0.04
Deviation from set Z-step [mm]	+0.07	−0.08	−0.01	+0.02	−0.12

Table 2 reports the average molten pool height and the deviation from the set Z-step (excluding the first layer from the computation). The two figures are different representations of the same phenomenon and highlight the problem under two points of view. A stable condition would appear in Fig. 10 as a horizontal line, representing a well maintained SOD layer after layer, and in Fig. 11 it would appear as points lying on the red reference line, meaning that the set Z-step is equal to the generated molten pool height and the obtained layer thickness. A positive or negative mismatch between the obtained molten pool height and the set Z-step in Fig. 11would result in a diminishing or increasing SOD in Fig. 10, respectively. Considering these two graphs and the table, one can assign the five tested process conditions to the three above-mentioned categories: undergrowth, overgrowth, and stable growth. The samples realized with the combination of process parameters that generates the highest linear energy density (blue line in Fig. 10 and in Fig. 11) are growing more than expected: the molten pool height is always slightly higher than the set Z-step, and this positive mismatch is accumulating layer after layer, making the SOD to reduce. On the contrary, the samples realized with the combination of process parameters that generates the lower linear energy density (green line in Fig. 10 and in Fig. 11) are growing less than expected: the molten pool height is always lower than the set Z-step, and this negative mismatch is accumulating layer after layer, making the SOD to increase. Considering the conditions that are characterized by the middle level of linear energy density, the printed samples do not show the same behavior, despite their having been produced with the same linear energy density. In fact, the samples that were realized with a combination of both high laser power and scan speed (dark orange line in Fig. 10 and in Fig. 11) were growing less than expected, whereas the other two conditions generated stable samples. Analyzing more in-depth the molten pool height records of the samples realized with the central point condition (yellow line in Fig. 10 and in Fig. 11), they are always slightly lower than the set Z-step, and the SOD is slightly increasing layer after layer. However, for the fifteen layers realized, the condition can be considered stable. The standard deviation of the measured SOD is high in all the tested conditions and for every layer, thus suggesting an intense variation of the SOD within each layer. The oscillations seem to be more pronounced in the overgrowing samples compared to the other process conditions. The central point condition is certainly the less oscillating one, which remarks the high stability of the process with that set of process parameters. In addition, looking at Fig. 11 it seems that the molten pool height is oscillating a lot between the layers, especially in the purple and blue conditions. However, an important aspect of these measurements should be pointed out: the coaxial triangulator system is strongly affected by the positioning and in-trajectory accuracy and precision of the robot, and finally by its vibrations. Moreover, also the molten pool is characterized by its own dynamics that may interfere with the reflection of the green laser probe. For this reason, the need for applying the low-pass filter with a 5 layers cut-off on the acquired signal arose. The standard deviation of the molten pool height signal is not reported in the graph of Fig. 11 for reasons of clarity. Indeed, it has the same amplitude of the standard deviation of the SOD signal, which is dimensionally similar to the actual median value of the molten pool height.

Fig. 12 shows a randomly selected molten pool picture for every process condition, captured by the coaxial NIR camera. The correspondent segmented images, obtained with the procedure described in paragraph 2.5, are reported below the NIR pictures. The graph of Fig. 13 shows the records of the molten pool area of the five tested conditions for all the fifteen layers. Similarly to what happens with the SOD measured by the triangulator, the most and least energetic conditions are easily discriminated as the conditions with the widest and the tiniest molten pool, respectively. In particular, the molten pool generated by the combination of the highest laser power and the lowest scan speed (blue) is almost twice as large as the one generated by the combination of the lowest laser power and the highest scan speed (green). The areas of the molten pools generated by the three equally energetic conditions are between the two extrema conditions. By considering their distribution, it is reasonable to state that the influence of the laser power on the molten pool area prevails over the effect provided by the scan speed. In fact, the condition that is characterized by the combination of high power and high scan speed (dark orange) generates the largest molten pools among the three equally energetic conditions. Moreover, the molten pools that are obtained with this process condition are almost as largest as the ones that are obtained with the most energetic condition, attesting that an increment of 4 mm/s (from 10 mm/s) in the scan speed led to a shrinkage of the molten pool of just around 0.28 mm^2 (~6 %).

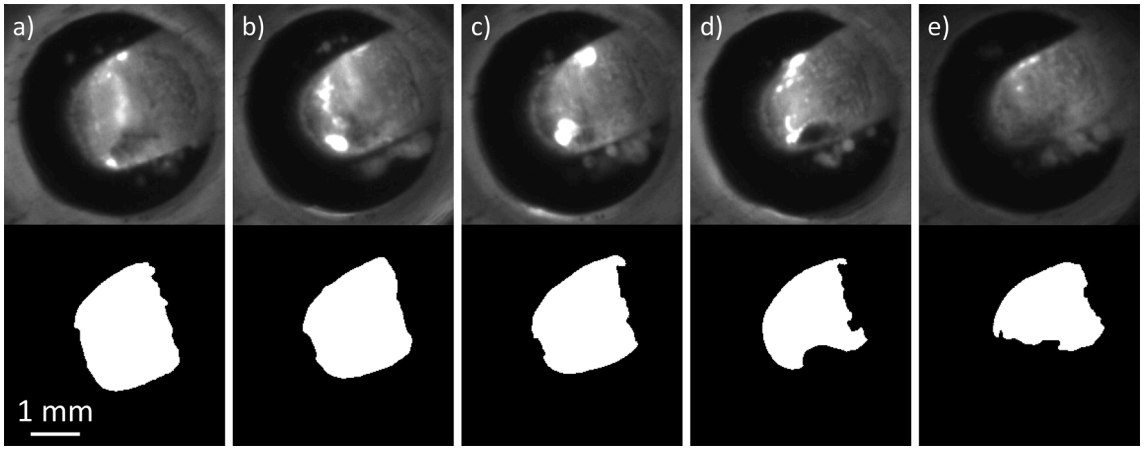

Fig. 12. Randomly selected pictures of the molten pools that are generated by the five tested process conditions and acquired by the coaxial NIR camera (above), with the result of the binarization procedure (below): a) P = 1000 W, v = 10 mm/s; b) P = 1000 W, v = 14 mm/s; c) P = 850 W, v = 12 mm/s; d) P = 700 W, v = 10 mm/s; e) P = 700 W, v = 14 mm/s.

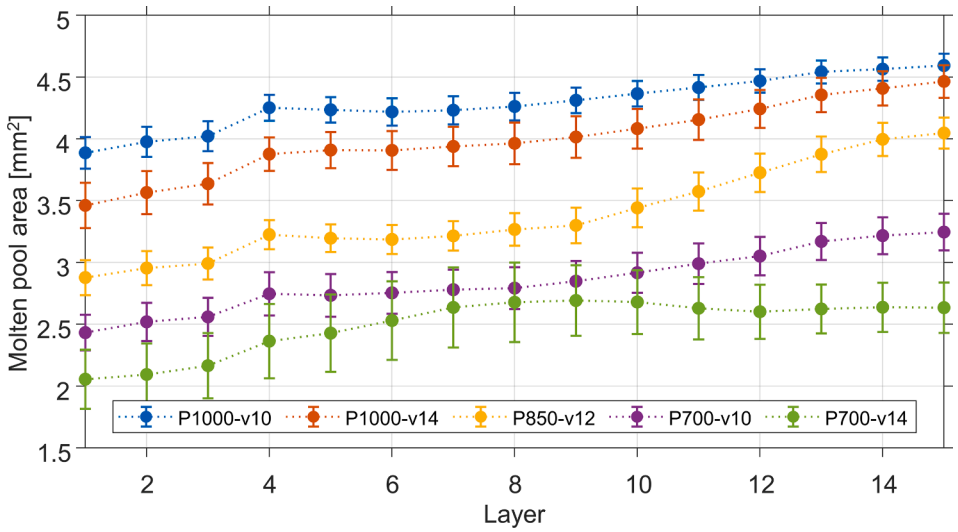

Fig. 13. Median molten pool area for every layer (error bars represent the temperature standard deviation within the layer).

Instead, the process condition that is characterized by the combination of low laser power and low scan speed (purple) generates the tiniest molten pools among the equally energetic conditions, showing that a reduction of 300 W (from 1000 W) of the laser power makes the molten pool to shrink of about 1.4 mm^2 (~33 %). The molten pools generated by the central point condition (yellow) are characterized by a medium area with respect to the other corner conditions. Another noticeable aspect that can be observed in Fig. 13 is that the detected molten pool is continuously growing, layer after layer, in all the five tested conditions. Only the least energetic condition reaches a plateau after few layers.

Fig. 14 shows the molten pool temperature of the five tested conditions for every layers. The condition characterized by the highest linear energy density (blue line in Fig. 13) is the hottest one, with an average molten pool temperature of 1840 °C. On the contrary, the condition characterized by the lowest linear energy density (green line in Fig. 13) is the colder one, with an average molten pool temperature of 1635 °C. The records of the three different conditions that produced the middle level of linear energy density generated molten pool temperatures ranging in between the two extrema. However, similarly to what was highlighted about the SOD and molten pool area, an equal value of energy density does not cause the same molten pool temperature. Indeed, the samples realized with the high level of laser power and the high level of scan speed (red line in Fig. 13) have higher molten pool temperature than the sample realized with the low level of power and the low level of scan speed (purple line in Fig. 13). The specimens that were realized with the central point condition (yellow line in Fig. 13) are characterized by a temperature that is in between the other corner conditions. The temperature signal shows a static trend in the blue, orange, and green conditions, while it shows a slightly upward trend layer after layer in the yellow and purple ones, with a plateau after few layers. The temperature of the central point condition reaches almost the same level of the high power/high scan speed one, thus suggesting a non-linear relationship between the input process parameters and the output temperature. Another aspect to be noticed in the graph is the very limited variation of the temperature within the layers, suggested by the very low standard deviation in all the tested conditions and for every layer.

To better summarize the previously exposed results, mean effect plots and interaction plots of molten pool height, molten pool area and temperature are reported in Fig. 15. With these graphs, the mean effect of the single process parameters and of their interaction can be easily assessed by looking at the displayed trends. The strong influence of the scan speed on the molten pool height as well as that of the laser power on the molten pool area and the temperature are particularly clear.

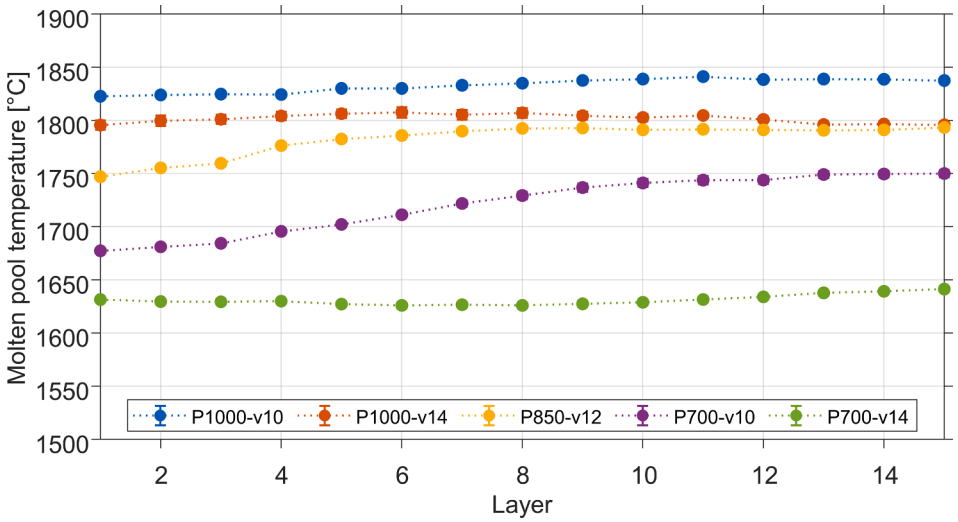

Fig. 14. Median molten pool temperature for every layer (error bars represent the temperature standard deviation within the layer).

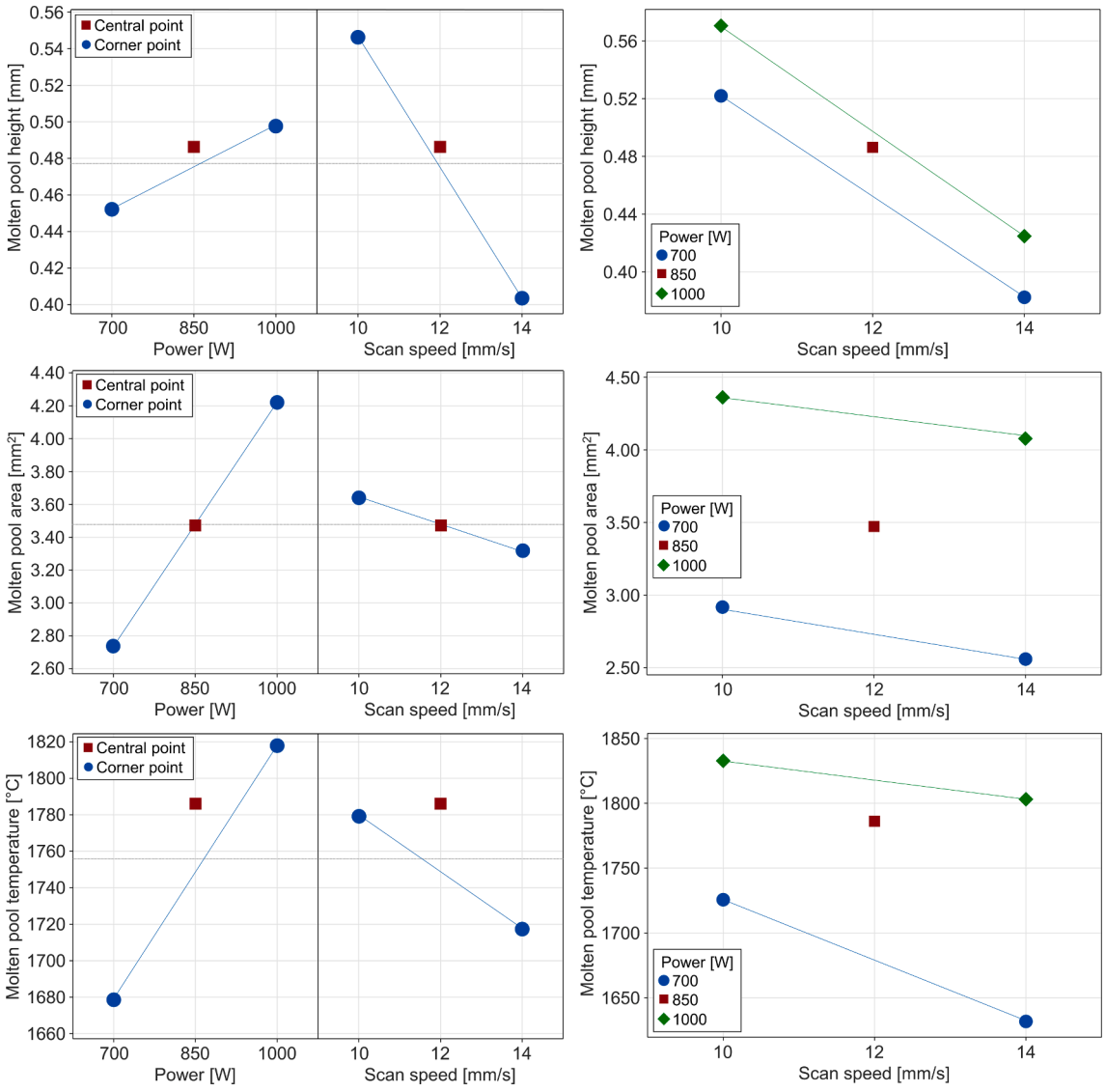

Fig. 15. Main effect plots (left column) and interaction plots (right column) of molten pool height, molten pool area and temperature.

Table 3
ANOVA table for molten pool height.

Source	DF	Adj SS	Adj MS	F-Value	P-Value
Model	17	0.99613	0.058596	26.57	0.000
Layers	13	0.22062	0.016971	7.70	0.000
Linear	2	0.78150	0.390752	177.22	0.000
Power [W]	1	0.06861	0.068613	31.12	0.000
Scan speed [mm/s]	1	0.71271	0.712710	323.23	0.000
2-Way Interactions	1	0.00044	0.000445	0.20	0.654
Power [W]*Scan speed [mm/s]	1	0.00044	0.000445	0.20	0.654
Curvature	1	0.00664	0.006641	3.01	0.084
Error	186	0.41012	0.002205		
Lack-of-Fit	52	0.13763	0.002647	1.30	0.117
Pure Error	134	0.27249	0.002034		
Total	203	1.40625			

Table 4
ANOVA table for molten pool area.

Source	DF	Adj SS	Adj MS	F-Value	P-Value
Model	17	104.417	6.1422	138.09	0.000
Layers	13	8.924	0.6865	15.43	0.000
Linear	2	94.524	47.2622	1062.56	0.000
Power [W]	1	90.672	90.6722	2038.50	0.000
Scan speed [mm/s]	1	4.098	4.0977	92.12	0.000
2-Way Interactions	1	0.035	0.0353	0.79	0.374
Power [W]*Scan speed [mm/s]	1	0.035	0.0353	0.79	0.374
Curvature	1	0.004	0.0040	0.09	0.764
Error	191	8.496	0.0445		
Lack-of-Fit	52	2.799	0.0538	1.31	0.107
Pure Error	139	5.697	0.0410		
Total	208	112.913			

Additionally, the effects of also the other considered parameters (namely, the laser power on the molten pool height and the scan speed on the molten pool area and on the temperature) can be more easily appreciated than with the single graphs, and this cannot be neglected. On the other hand, no significant interaction between the laser power and the scan speed appears as obvious from the graphs.

Table 3, Table 4 and Table 5 are the ANOVA tables for the molten pool height, the molten pool area and the molten pool temperature, respectively. The analyses confirm what was observed on the graphs of Fig. 15. In fact, both the laser power and the scan speed are influencing

Table 5
ANOVA table for molten pool temperature.

Source	DF	Adj SS	Adj MS	F-Value	P-Value
Model	17	1,128,337	66,373	505.36	0.000
Layers	13	6071	467	3.56	0.000
Linear	2	1,030,441	515,221	3922.90	0.000
Power [W]	1	848,899	848,899	6463.53	0.000
Scan speed [mm/s]	1	74,681	74,681	568.62	0.000
2-Way Interactions	1	15,821	15,821	120.46	0.000
Power [W]*Scan speed [mm/s]	1	15,821	15,821	120.46	0.000
Curvature	1	55,874	55,874	425.42	0.000
Error	171	22,459	131		
Lack-of-Fit	51	7855	154	1.27	0.149
Pure Error	120	14,604	122		
Total	188	1,150,796			

all the three outputs. The F-Values state that the scan speed has the most important effect on the molten pool height and that the laser power is the most influent on the molten pool area and temperature. Furthermore, the significative effect of the interaction between the laser power and the scan speed on the molten pool temperature is also spotted by the analysis. The curvature emerges as significative in the analysis of the molten pool temperature, suggesting a non-linear relationship between the molten temperature and the input parameters. The adjusted coefficients of determination R^2_{adj} of the molten pool height, area and temperature analyses are 68.17%, 91.81%, and 97.85%, respectively. These are very high in all analyses, suggesting a remarkable goodness-of-fit of the three proposed models. The coefficient of determination of the molten pool height model is lower than the ones of the other two. This can be attributed to the higher variability of the measurements taken with the triangulator with respect to the ones acquired with the NIR camera and the pyrometer. In all the three analyses, the lack of fit is not significant, and the standardized residuals are normally distributed.

The scatterplot between the molten pool height and the temperature is reported in Fig. 16, where the points correspond to every layer of every sample (the first layer is neglected). The points are scattered in the graph, and the five conditions are not well aligned. The line of best fit between the temperature and the molten pool height is plotted on top of the points, as well as the 95% confidence interval (CI) and the 95% prediction interval (PI). The Pearson correlation coefficient is 0.429 (confidence interval: 0.311-0.534, p-value < 0.05), suggesting a weak linear correlation between the molten pool height and its temperature in the considered parameter ranges. The number of layers has no discernible effect.

Similarly to the previous figure, the relationship between the molten pool area and the temperature is depicted in the scatter plot of Fig. 17 (the first layer is omitted). In this case, the five tested conditions are well separated and identified in the graph, and they are also well aligned. The line of best fit between the temperature and the molten pool area is plotted on top of the points, as well as the 95% confidence interval (CI) and the 95% prediction interval (PI). the Pearson correlation coefficient is 0.848 (confidence interval: 0.805-0.882, p–value< 0.05), suggesting a strong linear correlation between the two considered output variables. Looking at the plot, unlikely in the previous case, it is possible to also appreciate the effect of the layers. In fact, in most of the cases, the molten pool enlarges at higher layers, while the temperature is not so much affected. This result is following what was observed in Fig. 13 and Fig. 14.

4. Discussion

The described experimental campaign allows to analyze of the effect of two of the principal process parameters of LMD, i.e., the laser power and the scan speed, on three in-situ monitored outputs, i.e., the molten pool height and the SOD, the molten pool area, and the molten pool temperature. The deposited layer height is considered equal to the molten pool height. Through the first considered sensor, which is the coaxial triangulator, the current SOD can be measured to detect overgrowth and undergrowth flaws. In the tested parameter ranges, both defects occurred, generating samples that resulted to be higher and lower than expected, respectively. The final component height is the result of the sum of the height of each layer, and even a small difference between the set Z-step and the actual deposited layer thickness leads to the final macro-defect. In the case of overgrowth, the self-stabilizing phenomenon will take place after a certain number of layers, preventing an excessive reduction of the SOD. The self-stabilizing phenomenon occurs due to a reduction of the powder catchment efficiency with respect to the initial layers, as explained in [58–60]. For this reason, even if this type of defect will not determine the failure of the build, it is still a drift from the designed process conditions, and it should be avoided. On the other hand, the undergrowth defect will only accumulate layer after layer, eventually determining the lack of growth of the component. From the measurements obtained with the coaxial triangulator, the scan speed emerges as more impactful than the laser power on the molten pool height, according to the ANOVA analysis of Table 3. Considering for example the least energetic condition, i.e., the one characterized by the lowest laser power and the highest scan speed,

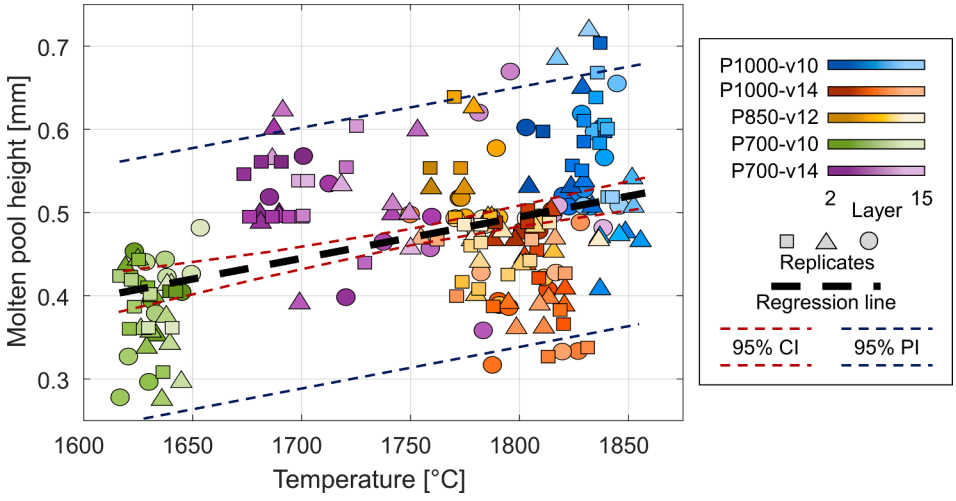

Fig. 16. Relationship between the molten pool height and the temperature for every parameter combination. The black dashed line is the line of best fit between the temperature and the molten pool height.

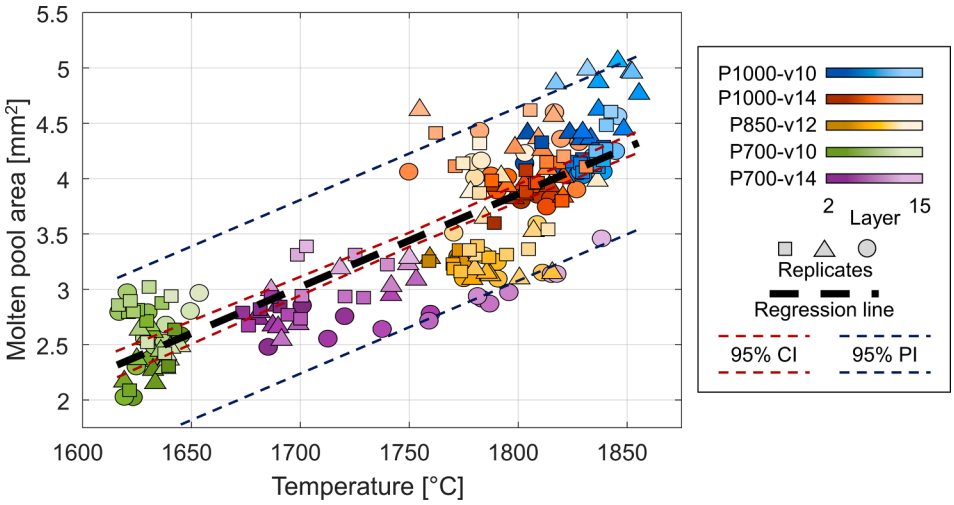

Fig. 17. Relationship between the molten pool area and the temperature for every parameter combination. The black dashed line is the line of best fit between the temperature and the molten pool area.

the component is growing less than expected, thus determining remarkable undergrowth. In order to correct the defect, one could increase the input energy by either operating on the laser power or on the scan speed, by rising or reducing them, respectively. Given the results (Fig. 10), the former solution is not sufficient to solve the undergrowth problem, while the latter is able to make the build stable. There is an influence of the laser power on the molten pool height, but the response is weaker than the one induced by the scan speed, considering isoenergetic conditions. However, it cannot be stated by this experiments that adding even more laser power to the molten pool will fix the undergrowth issue. The best choice to avoid overgrowth and undergrowth problems during the builds would be to consider the Z-step as a process parameter dependent on the combination of laser power and scan speed, trying to match it to the layer thickness generated by them. However, this may not be always possible, since the scan speed cannot always be kept under control: discontinuities in the scanning direction, for example in the case of a corner or a low-radius fillet in the tool path, make the scan speed to unavoidably decrease. Material and heat accumulate in such points, locally increasing the layer thickness. It may be possible to prevent this kind of defect by providing for power ramps, synchronized with the current scan speed; however, this option may not be applicable in the case of multi-pass depositions, and requires an extensive preliminary experimental campaign to characterize the deposited track height for various combinations of laser power and scan speed.

The molten pool height measured by means of the coaxial triangulator is a direct index of the final height of the deposited track. Similarly, the molten pool area measurement by means of the NIR coaxial camera is a direct index of the final width of the deposited track/wall. Based on the experimental campaign carried out, it is possible to state that the laser power is more effective on the molten pool area variation than the scan speed, since considering a constant energy density level, the combination of high power and high scan speed are characterized by a larger molten pool than in the case of low laser power and low scan speed (Fig. 15 and Table 4). The same response to the variation of these two process parameters is observed on the molten pool temperature measured with the ratio pyrometer (Fig. 15 and Table 5): the temperature is more affected by the laser power than by the scan speed. The graph of Fig. 17 and the related correlation analysis exposes a good linear relationship between the two considered outputs that is supported by a high coefficient of determination. Hence, it may be possible to predict with a good approximation the molten pool area by knowing the molten pool temperature. For this reason, the molten pool temperature can be considered an indirect estimator of deposited track width. However, a drawback of this evidence is that the two process signatures cannot be controlled in a mutually independent way by acting on the laser power and on the scan speed. On the contrary, due to the different response to the inputs of the molten pool height, this can be controlled almost independently from the molten pool area and temperature. This fact can be deduced by Fig. 16 and by its related correlation analysis, where the molten pool height and the temperature are put into relationship. The Pearson correlation coefficient between the molten pool temperature and its height is low, thus confirming the weak correlation between them. The proposed analyses are a preliminary work to establish the controllability of the LMD process using the three proposed coaxial sensors.

The coaxial setup of the monitoring system allows the simultaneous extraction of the process signatures from the molten pool, and allowed the assessment of correlations between the sensed process signatures. This configuration is suitable to be implemented as a feedback control system, since all the information is acquired in real-time and are referred to the current status of the process. Thanks to the presented experimental campaign, it is possible to outline an effective and efficient control strategy to manipulate the three considered process signatures (molten pool height, molten pool area and molten pool temperature) with the two tested inputs (laser power and scan speed). The ANOVAs of Table 3, Table 4 and Table 5 assess the effect of the controllable (laser power and scan speed) and uncontrollable (layers) parameters on the process signatures, and the correlation analyses highlight the relationships between the process signatures. With these bases, targeted experimental campaigns can be designed to find the complete regression models to be implemented in a feedback control system.

Furthermore, considerations about the data acquisition and manipulation should also be made to select the best setup. In this work, the monitoring of the molten pool area and of the SOD is demanded to camera-based systems. Due to the higher dimensionality of the data acquired by cameras than the data acquired by pyrometers, these two variables are harder to be monitored since require imaging elaboration procedures which in their turn require the development of a proper data elaboration algorithm. Furthermore, the cameras are equipped with only one sensor, and for this reason the quality of the acquired images is strongly influenced by the emissivity and reflectivity properties of the molten pool during the deposition, which are in turn affected by the metal chemistry and temperature. This requires an intense preliminary experimentation that should be performed for every new material, in order to tune the acquisition and algorithm parameters. In the case of this work, the set framerate for the two camera-based systems is very low to allow good quality acquisitions. Nevertheless, molten pool height

and area signals were considerably oscillating. For example, the standard deviation of the molten pool height within a layer is comparable to its own median value, meaning that a closed-loop control based on this output would be very slow, with the consequent need to integrate the signal over a long time before acting for correction. Nowadays, pyrometry is a very well-established technology in various industrial fields, and high-speed ratio pyrometers are widely available on the market. Ratio pyrometers directly output the measured temperature, with no need for further elaboration. The only maintenance action that is required is a once-in-a-while calibration procedure on a blackbody source that is valid for every metallic material, which makes the pyrometer an almost plug-and-play device. Furthermore, some pyrometers are equipped with integrated PID controllers, allowing for a direct implementation for feedbacking the process. Considering the results of the presented experimental campaign, the temperature measured by the pyrometer is also the less oscillating of the output variables, and this observation plus the high refresh rate of the device allow for a rapid and precise control of the molten pool temperature.

Given the obtained results, it is possible to state that for controlling the molten pool height it would be convenient to close the loop on the scan speed. The feedback control of the molten pool height in the LMD process could be useful when using a non-layerwise slicing strategy, such as in the case of non-uniform Z-step within a layer. In such cases, on some machines it would be possible to calculate a variable scan speed at CAM level to compensate to this circumstance. Despite this possibility, an active feedback control may be more convenient, since it does not require previous experimentations to link the process parameters to the deposited track height, and it would work even with laterally overlapping tracks. However, the on-line measurement of the molten pool height or of the SOD is arguably a complex procedure due to multiple factors. First, the deposition head is placed at the end of a long kinematic chain that is the motion system of the machine, represented in this case by a 6-axis anthropomorphic robot. For this reason, the vibrations and positioning/trajectory inaccuracies of the robot may be badly affecting the SOD measurements made by a coaxial device. Furthermore, the camera-based laser triangulation device employed in this work introduces more complexity levels in the problem of measuring the molten pool height, and the dynamic of the molten pool also introduces noise in the measurement. Summing up all the effects, the oscillations in the output signal are significant: their amplitude is dimensionally similar to the median molten pool height itself. For this reason, the active control of the molten pool height may be too slow to be actually effective. Furthermore, thanks to the self-regulating effect that is typical of the LMD process, a wise selection of the Z-step would make the active control of the molten pool height not useful.

On the other hand, the feedback loop should be closed on the laser power for effectively controlling the molten pool area and temperature. The active control of the laser power is for sure faster than the control of the scan speed, being the laser source response time to the analog control input lower than 120 μs. The control of the temperature may affect the solidification rate of the deposited track [61] and so its final microstructure in the as-built state, while the molten pool area is an index of the solidified track final width. The molten pool area and the temperature were found to be significantly correlated between each other (Fig. 17). For this reason, the two are not independent and cannot be separately controlled. This evidence opens to the possibility of closing the loop between only one of the two outputs and the laser power, and this configuration would be effective on both the outputs. As an example, one can close the loop between the temperature measured by the pyrometer and, thanks to the proven strong linear correlation between the temperature and the molten pool area, use the strategy to actively control the area. This configuration is more convenient than using the direct loop with the NIR camera, due to the limitations and difficulties of usage of camera-based systems described in the previous paragraphs: the pyrometer is for sure the simpler and more reliable sensor for monitoring the molten pool, even without considering the fact that the adopted device in the tested setup is equipped with an integrated and configurable PID controller. Finally, as already discussed in this chapter, there are instances where the scan speed may not be consistent, like for example in the case of a corner or a low-radius fillet in the tool path. In such situations, the scan speed will unavoidably decrease, thus resulting in an accumulation of material and heat in those points. In these spots, the pyrometer would act against the heat accumulation by reducing the laser power, with the effect of maintaining a limited molten pool area and preventing an excessive thickening of the track.

5. Conclusions

A custom laser triangulation system, a NIR camera and a ratio pyrometer were coaxially implemented on the LMD deposition head to measure the molten pool height, area, and temperature, respectively. An experimental campaign on thin wall samples was conducted by varying the laser power and the scan speed to investigate their effect on the measured outputs. Correlation analyses were carried out between the sensed variables to find any relationship between them that can improve and simplify the monitoring architecture. Finding the ideal combinations within and between inputs and outputs and proposing the basic rules for effectively and efficiently controlling the LMD process was the goal of the work.

- The signals recorded by the two camera-based systems are very noisy and affected by external factors. The ratio pyrometer measures the molten pool temperature independently from the deposited material nature, it is simple to use and almost free of noise.
- The SOD and the molten pool height are more affected by the scan speed, while the molten pool area and temperature are more affected by the laser power. The latter two outputs are linearly correlated.
- The control of the molten pool height using the coaxial triangulator acting on the scan speed may be useful in the case of non-layerwise slicing strategy, in absence of a previous adaptive calculation of the scan speed based on the path program. However, its implementation may be not straightforward and not fast enough to react to defects.
- The relationship between the molten pool area and temperature may allow regulation of the area by controlling the laser power with a temperature-sensing pyrometer. A feedback loop between temperature and laser power can mitigate defects caused by reducing scan speed during corners or low radius fillets.

The analysis was possible thanks to the developed multi-sensor monitoring setup, which is able of providing real-time information about the process status and quality. The setup is powerful as it collects multiple pieces of information directly from the molten pool. The good correlation between the molten pool area and temperature may allow the simplification of the monitoring system with one sensor between the pyrometer and NIR camera. The suggestion for process control is to use a coaxial ratio pyrometer to control temperature by adjusting laser power and a coaxial triangulator to control the molten pool height by manipulating the scan speed.

The approach was applied and validated on straight thin-walled samples, and it should be extended to massive components with future experimentations. This was a preliminary work to investigate the capabilities of the proposed monitoring system, and to establish the basic rules for designing a feedback control system based on the chosen sensors. The relationship between the molten pool temperature and area will also be further investigated with a specific experimental campaign to find a proper predictive model between the two outputs.

CRediT authorship contribution statement

Simone Maffia: Conceptualization, Methodology, Investigation, Formal analysis, Software, Writing – original draft, Writing – review &

editing. **Valentina Furlan:** Conceptualization, Methodology, Writing – original draft. **Barbara Previtali:** Methodology, Writing – review & editing, Supervision, Funding acquisition.

Declaration of Competing Interest

The authors declare that they have no known competing financial interests or personal relationships that could have appeared to influence the work reported in this paper.

Data availability

Data will be made available on request.

Acknowledgements

Nuovo Pignone Tecnologie S.R.L. (Baker Hughes) is acknowledged for granting the industrial PhD scholarship under which this work was developed and for supplying the used materials. BLM S.P.A. (BLM Group) is acknowledged for the provided support through the supply of the used machine and monitoring equipment.

References

[1] W.E. Frazier, Metal additive manufacturing: a review, J. Mater. Eng. Perform. 23 (2014) 1917–1928, https://doi.org/10.1007/s11665-014-0958-z.
[2] P. Gradl, D.C. Tinker, A. Park, O.R. Mireles, M. Garcia, R. Wilkerson, C. Mckinney, Robust metal additive manufacturing process selection and development for aerospace components, J. Mater. Eng. Perform. 31 (8) (2022) 6013–6044, https://doi.org/10.1007/s11665-022-06850-0.
[3] L.E. Murr, E. Martinez, K.N. Amato, S.M. Gaytan, J. Hernandez, D.A. Ramirez, P. W. Shindo, F. Medina, R.B. Wicker, Fabrication of metal and alloy components by additive manufacturing: examples of 3d materials science, J. Mater. Res. Technol. 1 (2012) 42–54, https://doi.org/10.1016/S2238-7854(12)70009-1.
[4] T. Lehmann, D. Rose, E. Ranjbar, M. Ghasri-Khouzani, M. Tavakoli, H. Henein, T. Wolfe, A. Jawad Qureshi, Large-scale metal additive manufacturing: a holistic review of the state of the art and challenges, Int. Mater. Rev. 67 (4) (2022) 410–459, https://doi.org/10.1080/09506608.2021.1971427.
[5] B. Blakey-Milner, P. Gradl, G. Snedden, M. Brooks, J. Pitot, E. Lopez, M. Leary, F. Berto, A. du Plessis, Metal additive manufacturing in aerospace: A review, Mater. Des. 209 (2021), 110008, https://doi.org/10.1016/j.matdes.2021.110008.
[6] G. Bi, B. Schürmann, A. Gasser, K. Wissenbach, R. Poprawe, Development and qualification of a novel laser-cladding head with integrated sensors, Int. J. Mach. Tool Manu. 47 (2007) 555–561, https://doi.org/10.1016/j.ijmachtools.2006.05.010.
[7] M. Khanzadeh, S. Chowdhury, M.A. Tschopp, H.R. Doude, M. Marufuzzaman, L. Bian, In-situ monitoring of melt pool images for porosity prediction in directed energy deposition processes, IISE Trans. 51 (2019) 437–455, https://doi.org/10.1080/24725854.2017.1417656.
[8] J. Lee, H.J. Park, S. Chai, G.R. Kim, H. Yong, S.J. Bae, D. Kwon, Review on quality control methods in metal additive manufacturing, Appl. Sci. 11 (2021) 1966, https://doi.org/10.3390/app11041966.
[9] X. Wang, Z. Liu, Z. Guo, Y. Hu, A fundamental investigation on three–dimensional laser material deposition of AISI316L stainless steel, Opt. Laser Technol. 126 (2020), 106107, https://doi.org/10.1016/j.optlastec.2020.106107.
[10] I. Garmendia, J. Flores, M. Madarieta, A. Lamikiz, L.G. Uriarte, C. Soriano, Geometrical control of DED processes based on 3D scanning applied to the manufacture of complex parts, Proc. CIRP. 94 (2020) 425–429, https://doi.org/10.1016/j.procir.2020.09.158.
[11] M. Biegler, B.A.M. Elsner, B. Graf, M. Rethmeier, Geometric distortion-compensation via transient numerical simulation for directed energy deposition additive manufacturing, Sci. Technol. Weld. Join. (2020) 1–8, https://doi.org/10.1080/13621718.2020.1743927.
[12] X. Lin, K. Zhu, J.Y.H. Fuh, X. Duan, Metal-based additive manufacturing condition monitoring methods: From measurement to control, ISA Trans. 120 (2022) 147–166, https://doi.org/10.1016/j.isatra.2021.03.001.
[13] Z. Tang, W. Liu, Y. Wang, K.M. Saleheen, Z. Liu, S. Peng, Z. Zhang, H. Zhang, A review on in situ monitoring technology for directed energy deposition of metals, Int. J. Adv. Manuf. Technol. 108 (2020) 3437–3463, https://doi.org/10.1007/s00170-020-05569-3.
[14] G. Bi, A. Gasser, K. Wissenbach, A. Drenker, R. Poprawe, Identification and qualification of temperature signal for monitoring and control in laser cladding, Opt. Lasers Eng. 44 (2006) 1348–1359, https://doi.org/10.1016/j.optlaseng.2006.01.009.
[15] L. Song, F. Wang, S. Li, X. Han, Phase congruency melt pool edge extraction for laser additive manufacturing, J. Mater. Process. Technol. 250 (2017) 261–269, https://doi.org/10.1016/j.jmatprotec.2017.07.013.
[16] J. Rodriguez-Araujo, J.J. Rodriguez-andina, J. Farina, F. Vidal, J.L. Mato, M. A. Montealegre, Industrial laser cladding systems: FPGA-based adaptive control, IEEE Ind. Electron. Mag. 6 (2012) 35–46, https://doi.org/10.1109/MIE.2012.2221356.
[17] S. Ocylok, E. Alexeev, S. Mann, A. Weisheit, K. Wissenbach, I. Kelbassa, Correlations of melt pool geometry and process parameters during laser metal deposition by coaxial process monitoring, Phys. Proc. 56 (2014) 228–238, https://doi.org/10.1016/j.phpro.2014.08.167.
[18] J.T. Hofman, B. Pathiraj, J. van Dijk, D.F. de Lange, J. Meijer, A camera based feedback control strategy for the laser cladding process, J. Mater. Process. Technol. 212 (2012) 2455–2462, https://doi.org/10.1016/j.jmatprotec.2012.06.027.
[19] S. Moralejo, X. Penaranda, S. Nieto, A. Barrios, I. Arrizubieta, I. Tabernero, J. Figueras, A feedforward controller for tuning laser cladding melt pool geometry in real time, Int. J. Adv. Manuf. Technol. 89 (2017) 821–831, https://doi.org/10.1007/s00170-016-9138-7.
[20] Y. Liu, L. Wang, M. Brandt, An accurate and real-time melt pool dimension measurement method for laser direct metal deposition, Int. J. Adv. Manuf. Technol. 114 (7-8) (2021) 2421–2432, https://doi.org/10.1007/s00170-021-06911-z.
[21] J.S. Medina, W. Devesse, J. Ertveldt, P. Guillaume, Comparison of visual and hyperspectral monitoring of the melt pool during Laser Metal Deposition, Proc. CIRP. 94 (2020) 462–468, https://doi.org/10.1016/j.procir.2020.09.165.
[22] V. Errico, S.L. Campanelli, A. Angelastro, M. Dassisti, M. Mazzarisi, C. Bonserio, Coaxial monitoring of AISI 316L thin walls fabricated by direct metal laser deposition, Materials. 14 (2021) 673, https://doi.org/10.3390/ma14030673.
[23] R. Sampson, R. Lancaster, M. Sutcliffe, D. Carswell, C. Hauser, J. Barras, An improved methodology of melt pool monitoring of direct energy deposition processes, Opt. Laser Technol. 127 (2020), 106194, https://doi.org/10.1016/j.optlastec.2020.106194.
[24] H.-W. Hsu, Y.-L. Lo, M.-H. Lee, Vision-based inspection system for cladding height measurement in Direct Energy Deposition (DED), Addit. Manuf. 27 (2019) 372–378, https://doi.org/10.1016/j.addma.2019.03.017.
[25] S. Donadello, M. Motta, A.G. Demir, B. Previtali, Monitoring of laser metal deposition height by means of coaxial laser triangulation, Opt. Lasers Eng. 112 (2019) 136–144, https://doi.org/10.1016/j.optlaseng.2018.09.012.
[26] S. Donadello, M. Motta, A.G. Demir, B. Previtali, Coaxial laser triangulation for height monitoring in laser metal deposition, Proc. CIRP. 74 (2018) 144–148, https://doi.org/10.1016/j.procir.2018.08.066.
[27] I. Smurov, M. Doubenskaia, A. Zaitsev, Comprehensive analysis of laser cladding by means of optical diagnostics and numerical simulation, Surf. Coat. Technol. 220 (2013) 112–121, https://doi.org/10.1016/j.surfcoat.2012.10.053.
[28] D.A. Kriczky, J. Irwin, E.W. Reutzel, P. Michaleris, A.R. Nassar, J. Craig, 3D spatial reconstruction of thermal characteristics in directed energy deposition through optical thermal imaging, J. Mater. Process. Technol. 221 (2015) 172–186, https://doi.org/10.1016/j.jmatprotec.2015.02.021.
[29] M. Lison, W. Devesse, D. de Baere, M. Hinderdael, P. Guillaume, Hyperspectral and thermal temperature estimation during laser cladding, J. Laser Appl. 31 (2) (2019) 022313, https://doi.org/10.2351/1.5096129.
[30] J.J. Hammell, C.J. Ludvigson, M.A. Langerman, J.W. Sears, Thermal imaging of laser powder deposition for process diagnostics, in: American Society of Mechanical Engineers Digital Collection, 2012: pp. 41–48. https://doi.org/10.1115/IMECE2011-63701.
[31] Z. Yan, W. Liu, Z. Tang, X. Liu, N. Zhang, Z. Wang, H. Zhang, Effect of thermal characteristics on distortion in laser cladding of AISI 316L, J. Manuf. Process. 44 (2019) 309–318, https://doi.org/10.1016/j.jmapro.2019.06.011.
[32] M.H. Farshidianfar, A. Khajepour, A.P. Gerlich, Effect of real-time cooling rate on microstructure in Laser Additive Manufacturing, J. Mater. Process. Technol. 231 (2016) 468–478, https://doi.org/10.1016/j.jmatprotec.2016.01.017.
[33] M.H. Farshidianfar, A. Khajepour, A. Gerlich, Real-time control of microstructure in laser additive manufacturing, Int. J. Adv. Manuf. Technol. 82 (2016) 1173–1186, https://doi.org/10.1007/s00170-015-7423-5.
[34] S.J. Wolff, Z. Gan, S. Lin, J.L. Bennett, W. Yan, G. Hyatt, K.F. Ehmann, G.J. Wagner, W.K. Liu, J. Cao, Experimentally validated predictions of thermal history and microhardness in laser-deposited Inconel 718 on carbon steel, Addit. Manuf. 27 (2019) 540–551, https://doi.org/10.1016/j.addma.2019.03.019.
[35] M. Doubenskaia, M. Pavlov, S. Grigoriev, I. Smurov, Definition of brightness temperature and restoration of true temperature in laser cladding using infrared camera, Surf. Coat. Technol. 220 (2013) 244–247, https://doi.org/10.1016/j.surfcoat.2012.10.044.
[36] L. Song, V. Bagavath-Singh, B. Dutta, J. Mazumder, Control of melt pool temperature and deposition height during direct metal deposition process, Int. J. Adv. Manuf. Technol. 58 (2012) 247–256, https://doi.org/10.1007/s00170-011-3395-2.
[37] L. Song, J. Mazumder, Feedback control of melt pool temperature during laser cladding process, IEEE Trans. Control Syst. Technol. 19 (2011) 1349–1356, https://doi.org/10.1109/TCST.2010.2093901.
[38] H. Tan, J. Chen, F. Zhang, X. Lin, W. Huang, Estimation of laser solid forming process based on temperature measurement, Opt. Laser Technol. 42 (2010) 47–54, https://doi.org/10.1016/j.optlastec.2009.04.016.
[39] G. Muvvala, D. Patra Karmakar, A.K. Nath, Monitoring and assessment of tungsten carbide wettability in laser cladded metal matrix composite coating using an IR pyrometer, J. Alloy. Compd. 714 (2017) 514–521, https://doi.org/10.1016/j.jallcom.2017.04.254.
[40] L. Tang, R.G. Landers, Melt pool temperature control for laser metal deposition processes—Part II: layer-to-layer temperature control, J. Manuf. Sci. Eng. 132 (2010), https://doi.org/10.1115/1.4000883.
[41] L. Tang, R.G. Landers, Melt pool temperature control for laser metal deposition processes—Part I: online temperature control, J. Manuf. Sci. Eng. 132 (2010), https://doi.org/10.1115/1.4000882.

[42] M. Gipperich, J. Riepe, K. Arntz, T. Bergs, Pulsed laser influence on temperature distribution during dual beam laser metal deposition, Metals. 10 (2020) 766, https://doi.org/10.3390/met10060766.
[43] Y. Wu, B. Cui, Y. Xiao, Crack detection during laser metal deposition by infrared monochrome pyrometer, Materials. 13 (2020) 5643, https://doi.org/10.3390/ma13245643.
[44] B. Müller, U. Renz, Development of a fast fiber-optic two-color pyrometer for the temperature measurement of surfaces with varying emissivities, Rev. Sci. Instrum. 72 (2001) 3366–3374, https://doi.org/10.1063/1.1384448.
[45] Y. Ding, J. Warton, R. Kovacevic, Development of sensing and control system for robotized laser-based direct metal addition system, Addit. Manuf. 10 (2016) 24–35, https://doi.org/10.1016/j.addma.2016.01.002.
[46] D. Hu, R. Kovacevic, Sensing, modeling and control for laser-based additive manufacturing, Int. J. Mach. Tool Manu. 43 (2003) 51–60, https://doi.org/10.1016/S0890-6955(02)00163-3.
[47] D. Hu, H. Mei, G. Tao, R. Kovacevic, Closed Loop Control of 3D Laser Cladding Based on Infrared Sensing, in: 2001. https://doi.org/10.26153/tsw/3245.
[48] Q. Deng, W. Fu, D. Chen, P. Cao, Measurement of the Molten Pool Image during Laser Cladding Process, in, Atlantis Press, 2014, pp. 630–634, https://doi.org/10.2991/meic-14.2014.141.
[49] G. Bi, C.N. Sun, A. Gasser, Study on influential factors for process monitoring and control in laser aided additive manufacturing, J. Mater. Process. Technol. 213 (2013) 463–468, https://doi.org/10.1016/j.jmatprotec.2012.10.006.
[50] G. Bi, A. Gasser, K. Wissenbach, A. Drenker, R. Poprawe, Characterization of the process control for the direct laser metallic powder deposition, Surf. Coat. Technol. 201 (2006) 2676–2683, https://doi.org/10.1016/j.surfcoat.2006.05.006.
[51] B.T. Gibson, Y.K. Bandari, B.S. Richardson, W.C. Henry, E.J. Vetland, T. W. Sundermann, L.J. Love, Melt pool size control through multiple closed-loop modalities in laser-wire directed energy deposition of Ti-6Al-4V, Addit. Manuf. 32 (2020), 100993, https://doi.org/10.1016/j.addma.2019.100993.
[52] T. Shi, B. Lu, T. Shen, R. Zhang, S. Shi, G. Fu, Closed-loop control of variable width deposition in laser metal deposition, Int. J. Adv. Manuf. Technol. 97 (2018) 4167–4178, https://doi.org/10.1007/s00170-018-1895-z.
[53] X. Cao, B. Ayalew, Robust multivariable predictive control for laser-aided powder deposition processes, J. Franklin Inst. 356 (2019) 2505–2529, https://doi.org/10.1016/j.jfranklin.2018.12.015.
[54] M. Akbari, R. Kovacevic, Closed loop control of melt pool width in robotized laser powder–directed energy deposition process, Int. J. Adv. Manuf. Technol. 104 (2019) 2887–2898, https://doi.org/10.1007/s00170-019-04195-y.
[55] J. Johansson, C. Persson, G. Testa, A. Ruggiero, N. Bonora, M., Hörnqvist Colliander, Effect of microstructure on dynamic shear localisation in Alloy 718, Mech. Mater. 109 (2017) 88–100, https://doi.org/10.1016/j.mechmat.2017.03.020.
[56] D. Paulonis, J.J. Schirra, Alloy 718 at Pratt & Whitney: Historical Perspective and Future Challenges, (2001). https://doi.org/10.7449/2001/Superalloys_2001_13_23.
[57] B02 Committee, Specification for Precipitation-Hardening and Cold Worked Nickel Alloy Bars, Forgings, and Forging Stock for Moderate or High Temperature Service, ASTM International, n.d. https://doi.org/10.1520/B0637-18.
[58] S. Donadello, V. Furlan, A.G. Demir, B. Previtali, Interplay between powder catchment efficiency and layer height in self-stabilized laser metal deposition, Opt. Lasers Eng. 149 (2022), 106817, https://doi.org/10.1016/j.optlaseng.2021.106817.
[59] P.-Y. Lin, F.-C. Shen, K.-T. Wu, S.-J. Hwang, H.-H. Lee, Process optimization for directed energy deposition of SS316L components, Int. J. Adv. Manuf. Technol. 111 (2020) 1387–1400, https://doi.org/10.1007/s00170-020-06113-z.
[60] J.C. Haley, B. Zheng, U.S. Bertoli, A.D. Dupuy, J.M. Schoenung, E.J. Lavernia, Working distance passive stability in laser directed energy deposition additive manufacturing, Mater. Des. 161 (2019) 86–94, https://doi.org/10.1016/j.matdes.2018.11.021.
[61] H. Wang, W. Liu, Z. Tang, Y. Wang, X. Mei, K.M. Saleheen, Z. Wang, H. Zhang, Review on adaptive control of laser-directed energy deposition, OE. 59 (2020), 070901, https://doi.org/10.1117/1.OE.59.7.070901.